Journal of Applied Physics

Characterization of ferroelectric domain walls by scanning electron microscopy

Cite as: J. Appl. Phys. **128**, 191102 (2020); https://doi.org/10.1063/5.0029284
Submitted: 11 September 2020 . Accepted: 21 October 2020 . Published Online: 17 November 2020

K. A. Hunnestad, E. D. Roede, A. T. J. van Helvoort, and D. Meier

COLLECTIONS

Paper published as part of the special topic on Domains and Domain Walls in Ferroic Materials DDWFM2021

This paper was selected as an Editor's Pick

ARTICLES YOU MAY BE INTERESTED IN

Contributions to polarization and polarization switching in antiphase boundaries of $SrTiO_3$ and $PbZrO_3$
Journal of Applied Physics **128**, 194101 (2020); https://doi.org/10.1063/5.0030038

III–V lasers selectively grown on (001) silicon
Journal of Applied Physics **128**, 200901 (2020); https://doi.org/10.1063/5.0029804

Tracking ferroelectric domain formation during epitaxial growth of $PbTiO_3$ films
Applied Physics Letters **117**, 132901 (2020); https://doi.org/10.1063/5.0021434

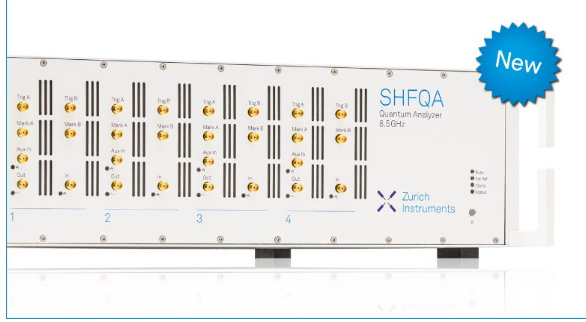

Your Qubits. Measured.
Meet the next generation of quantum analyzers
- Readout for up to 64 qubits
- Operation at up to 8.5 GHz, mixer-calibration-free
- Signal optimization with minimal latency

Find out more

© 2020 Author(s).

Journal of Applied Physics
TUTORIAL
scitation.org/journal/jap

Characterization of ferroelectric domain walls by scanning electron microscopy

Cite as: J. Appl. Phys. **128**, 191102 (2020); doi: 10.1063/5.0029284
Submitted: 11 September 2020 · Accepted: 21 October 2020 · Published Online: 17 November 2020

View Online

Export Citation

CrossMark

K. A. Hunnestad,[1] E. D. Roede,[1] A. T. J. van Helvoort,[2] and D. Meier[1,a)]

AFFILIATIONS

[1]Department of Materials Science and Engineering, Norwegian University of Science and Technology (NTNU), 7491 Trondheim, Norway
[2]Department of Physics, Norwegian University of Science and Technology (NTNU), 7491 Trondheim, Norway

Note: This paper is part of the Special Topic on Domains and Domain Walls in Ferroic Materials.
[a)]**Author to whom correspondence should be addressed:** dennis.meier@ntnu.no

ABSTRACT

Ferroelectric domain walls are a completely new type of functional interface, which have the potential to revolutionize nanotechnology. In addition to the emergent phenomena at domain walls, they are spatially mobile and can be injected, positioned, and deleted on demand, giving a new degree of flexibility that is not available at conventional interfaces. Progress in the field is closely linked to the development of modern microscopy methods, which are essential for studying their physical properties at the nanoscale. In this article, we discuss scanning electron microscopy (SEM) as a powerful and highly flexible imaging technique for scale-bridging studies on domain walls, continuously covering nano- to mesoscopic length scales. We review seminal SEM experiments on ferroelectric domains and domain walls, provide practical information on how to visualize them in modern SEMs, and provide a comprehensive overview of the models that have been proposed to explain the contrast formation in SEM. Going beyond basic imaging experiments, recent examples for nano-structuring and correlated microscopy work on ferroelectric domain walls are presented. Other techniques, such as 3D atom probe tomography, are particularly promising and may be combined with SEM in the future to investigate individual domain walls, providing new opportunities for tackling the complex nanoscale physics and defect chemistry at ferroelectric domain walls.

© 2020 Author(s). All article content, except where otherwise noted, is licensed under a Creative Commons Attribution (CC BY) license (http://creativecommons.org/licenses/by/4.0/). https://doi.org/10.1063/5.0029284

I. INTRODUCTION

The research on ferroelectric materials and phenomena has matured significantly since the discovery of ferroelectricity in Rochelle salt in 1920.[1] Today, ferroelectrics are used in different fields of technology, for instance, finding application in active damping units, capacitors, and random-access memories.[2] Despite the tremendous progress that has been made in understanding ferroelectrics, this class of materials keeps attracting attention as a rich source for new emergent properties, representing a fascinating playground for both fundamental and applied sciences. Recent examples include spin-driven ferroelectrics,[3] which facilitate a unique coupling between spin and lattice degrees of freedom,[4] as well as ferroelectric skyrmions and vortices,[5–7] representing new and intriguing states of matter. In this article, we will focus on the rapidly growing field of research that studies ferroelectric domain walls and their functionality.[8–11]

Due to the small length scales associated with ferroelectric domain walls, which usually have a width in the order of 1–10 nm,[11] progress in this field is closely related to advances in spatially resolved characterization methods.[12] Transmission electron microscopy (TEM) is nowadays readily applied to study the atomic-scale structure at ferroelectric domain walls,[13–15] and electron energy loss spectroscopy (EELS) provides insight into the local electronic and chemical properties.[16–19] At the nanoscale, scanning probe microscopy (SPM) methods, such as piezoresponse force microscopy (PFM)[20,21] and conductive atomic force microscopy (cAFM),[22,23] are routinely used to determine domain wall charge states and study their electronic transport behavior, respectively.[14,24–31] In addition, photoemission electron microscopy (PEEM)[32–35] and low-energy electron microscopy (LEEM)[36–39] have been explored to widen the accessible parameter space, mapping transport phenomena and electrostatic potentials with nanoscale spatial resolution.[40]

© Author(s) 2020

One of the most common characterization techniques that allows for spatially resolved measurements with nanometer scale resolution is scanning electron microscopy (SEM). As such, it is not surprising that SEM also plays a special role among the imaging techniques that have been applied in the research on ferroelectric domain walls. In the 1970s, SEM was used to image ferroelectric domain walls and gain insight into their unusual nanoscale physics.[41–43] Since then, the SEM technology has evolved considerably and, together with SPM, has turned into a mainstream technique for surface analysis. SEM has an outstanding—yet not fully exploited—potential for domain-wall related investigations, offering contact-free and non-destructive high-speed imaging, nanoscale spatial resolution, and a high flexibility in terms of specimen preparation and geometry that allows, for example, to combine microscopy with nano-structuring or *in situ*/*in operando* transport measurements.

In this Tutorial, we discuss the practical use of the SEM technique in connection with visualizing ferroelectric domains and domain walls. Mastering the ferroelectric contrast enables possibilities for combining SEM with other complementary techniques, such as SPM, TEM, and FIB (focused ion beam), opening new pathways for the investigation of the complex physics at domain walls and property monitoring in device-relevant geometries. We begin the Tutorial with an introduction to domain walls in ferroelectrics (Sec. I A) and typical characterization techniques applied to investigate them (Sec. I B). In Sec. II, the SEM technique is introduced; we begin with a history of SEM-based domain and domain wall imaging experiments (Sec. II A), followed by the basic operating principles (Sec. II B) and some practical advice for imaging ferroelectric domain walls (Sec. II C). In Sec. II D, we provide an overview of the different models used to explain the SEM contrast at neutral and charged domain walls. Sections III and IV are devoted to correlated techniques, considering SEM in combination with FIB. We discuss how SEM can be integrated/essential/correlated to other techniques such as TEM, SPM, and atom probe tomography (APT), respectively, with a focus on new possibilities for future domain wall research.

A. Domain walls in ferroelectrics

Ferroelectric materials exhibit a spontaneous polarization that can be switched by an external electric field.[44] Depending on the symmetry of the unit cell, ferroelectrics have at least two symmetrically equivalent directions for polarization. A region with a constant direction of the polarization is called a domain, and the domains are separated by a natural type of interface, that is, the "domain wall" (see Fig. 1 for a schematic illustration). Depending on the possible domain states, anisotropy and dipole–dipole interactions, there are different ways for the polar order to change across domain walls as discussed in detail in the comprehensive textbook by Tagantsev *et al.*[44] In $BiFeO_3$, for example, the polarization can point along any of the ⟨111⟩ directions in the rhombohedral unit cell, forming 71°, 90°, and 180° domain walls.[45] In prototypical ferroelectrics, such domain walls are pre-dominantly Ising-type walls, but more complex mixed structures are also possible, involving Bloch- or Néel-like rotations of the polarization vector.[46] Here, for simplicity, we will focus on 180° domain walls, where the polarization changes by 180° from one domain to the next, without discussing further details of the inner domain wall structure.

Within the category of 180° domain walls, we can further separate between three fundamental cases: The polarization P at the wall can either be in side-by-side (↑↓), head-to-head (→←), or tail-to-tail (←→) configuration as depicted in Figs. 1(a)–1(c). At head-to-head and tail-to-tail domain walls, the polarization has a component normal to the wall (div $P \neq 0$), which leads to the formation of bound charges.[47–49] These bound charges require screening, driving a redistribution of mobile charge carriers (ionic and/or electronic). Electrons, for example, are attracted by the positive electrostatic potential at head-to-head walls and repelled by the negative electrostatic potential at tail-to-tail domain walls. As a consequence of this redistribution, increased and reduced conductivities can be observed at charged ferroelectric domain walls.[26,29] However, the charge-driven mechanism described here is only one of the established mechanisms causing conduction. Other mechanisms include a reduction in the bandgap or formation of intra-bandgap states caused by defects at the walls (see, e.g., Refs. 50 and 51 for a review). In short, domain walls represent naturally occurring interfaces, which exhibit unique electronic properties different from the surrounding bulk, offering great potential as 2D systems for the development of the next-generation nanotechnology.[52]

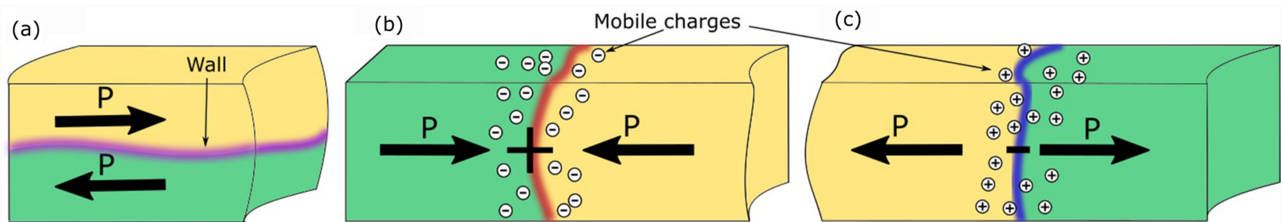

FIG. 1. Schematic illustration of the three fundamental types of ferroelectric 180° domain walls. (a) Neutral side-by-side domain wall (purple). Black arrows indicate the direction of the spontaneous polarization P in the adjacent domains (yellow and green). (b) Positively charged head-to-head domain wall (red). The associated domain wall bound charges (+) are screened by accumulating mobile charge carriers, which can either be electrons, negatively charges ions, or a combination of both. (c) Negatively charged tail-to-tail domain wall (blue). Negative bound charges (−) are screened by mobile positively charged carriers (electron holes and/or positively charged ions).

© Author(s) 2020

B. Spatially resolved measurements

To access all relevant length scales from atomically sharp domain walls to mesoscopic domains, a variety of microscopy techniques has been applied, as illustrated in Fig. 2. Historically, optical techniques with a resolution of about 1 μm were the primary option for ferroelectric domain imaging, nowadays reaching down to 200 nm in near-field optical microscopy.[53,54] Optical imaging was used, for example, to resolve domains in optically active materials, such as lead germanate ($Pb_5Ge_3O_{11}$)[55] and in combination with preferential chemical etching in hexagonal manganites ($YMnO_3$).[56] With the advent of modern microscopy methods, ferroelectric domains and domain walls in a much wider range of materials became accessible, facilitating a more comprehensive analysis. Figure 2 presents selected microscopy studies performed on the family of hexagonal manganites, which has evolved into one of the most intensively studied model systems in the field of domain wall nanoelectronics. Going beyond the resolution limit of classical optical microscopy measurements, the domain formation in hexagonal manganites and other ferroelectrics has been investigated by piezoresponse force microscopy (PFM).[57,58] The functional properties of domain walls, such as conductivity and magnetism, have been investigated by conductive-atomic force microscopy (c-AFM) and magnetic force microscopy (MFM), respectively.[26,59–61] At the atomic scale, transmission electron microscopy (TEM) allows for the direct observation of the atomic positions and can visualize the internal domain wall structure.[62–65] Thus, it is possible to cover all relevant length scales in spatially resolved measurements, ranging from exact atomic positions to the macroscopic correlation phenomena associated with domain walls. It is important to note, however, that the specimen requirements for the different microscopy methods are completely different, which can make correlated studies challenging.

SEM is a surface sensitive imaging technique that is highly flexible and has been proven to be a very powerful technique for the visualization of ferroelectric domains and domain walls. Compared to the other methods, SEM sticks out because of the remarkably large range of length scales it can cover as illustrated in Fig. 2. Due to this continuous coverage of nano- and macroscopic length scales, SEM is an explicitly promising tool for domain-wall related research, adding value regarding accessibility and the integration of other advanced characterization and nanostructuring methods as we will discuss in Secs. II–IV.

II. SCANNING ELECTRON MICROSCOPY—FUNDAMENTALS AND APPLICATION OPPORTUNITIES

A. Domain and domain wall imaging by SEM—A short history

The SEM as we know it today was invented by Zworykin *et al.* in 1942.[66] In 1965, SEMs became commercially available[67] and just two years later, the first paper on ferroelectric domain imaging in $BaTiO_3$ by SEM was published [Fig. 3(a)].[41] Since then, SEM has become a standard tool for many fields of surface science, as it can provide significantly higher resolution (≈1 nm) than optical measurements and can exploit diverse contrast mechanisms, such as topographic contrast, elemental contrast, and grain contrast (see the book on SEM by Reimer[68] for a detailed description).

An important breakthrough regarding the investigation of ferroelectrics by SEM was made by Le Bihan *et al.* in 1972.[85]

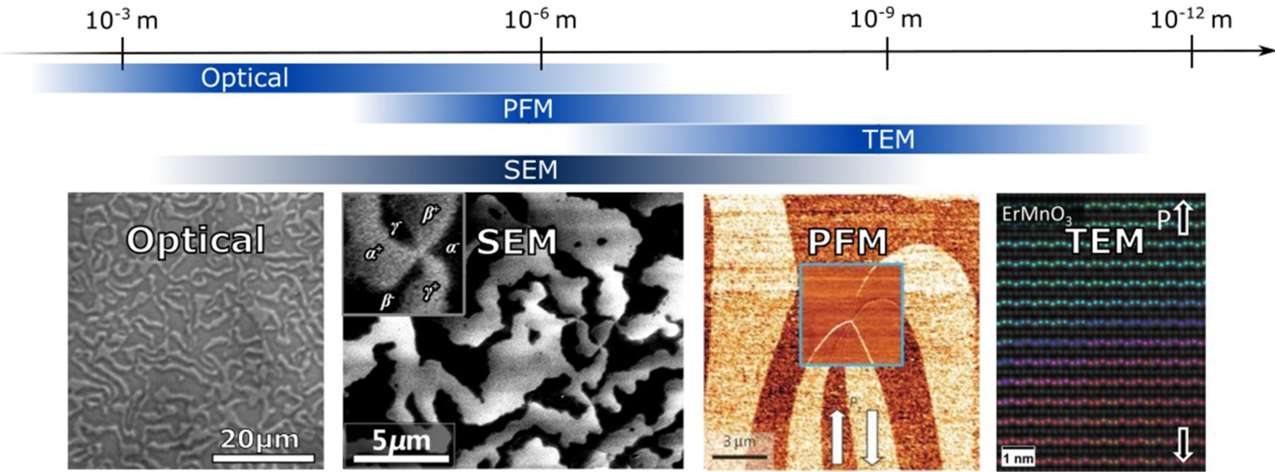

FIG. 2. Upper part: length scales covered by different characterization techniques that are regularly applied to investigate ferroelectric domains and domain walls. Lower part: examples of spatially resolved measurements of the ferroelectric domain structure in the hexagonal manganites, including optical microscopy, SEM, PFM, and TEM. In the two images on the left, bright and dark regions correspond to +P and −P domains with P oriented normal to the surface plane (out-of-plane polarization). In the two images on the right, P lies in the surface plane pointing in the directions indicated by the arrows (in-plane polarization). PFM and TEM images are adapted from Refs. 26 and 64. Optical image is reproduced with permission from Šafránková *et al.*, Czech. J. Phys. B **17**, 559 (1967). Copyright 1967 Springer Nature. SEM image is reproduced with permission from Li *et al.*, Appl. Phys. Lett. **100**, 152903 (2012). Copyright 2012 AIP Publishing LLC.

© Author(s) 2020

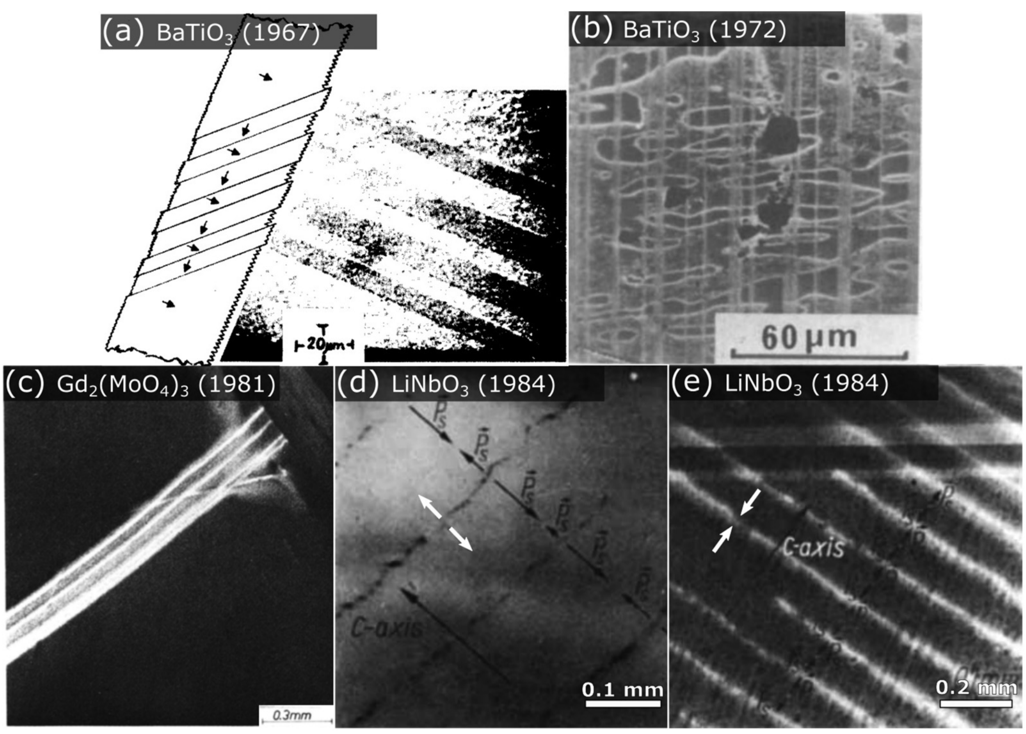

FIG. 3. Overview of seminal SEM-based studies on ferroelectric domains and domain walls. (a) First observation of SEM domain contrast in $BaTiO_3$, realized by selective etching and resulting topographic contrast. Bright and dark areas correspond to 90° domains as illustrated on the left. Black arrows indicate the polarization direction. Although such 90° domains and other variants are common in ferroelectrics, most SEM imaging studies have focused on 180° domains as presented in (c)–(e). Reproduced with permission from Robinson and White, Appl. Phys. Lett. **10**, 320 (1967). Copyright 1967 AIP Publishing LLC. (b) Observation of SEM contrast from ferroelectric domains (black and gray regions) and neutral domain walls (bright stripes) in $BaTiO_3$. The SEM data was recorded with low acceleration voltage (3 kV), removing the need for selective etching or specific coatings for imaging the domain distribution in ferroelectrics. Reproduced with permission from Le Bihan, Ferroelectrics **97**, 19 (1989). Copyright 1989 Taylor & Francis Ltd. (c) Observation of domain walls (bright stripes) in improper ferroelectric $Gd_2(MoO_4)_3$. Reproduced with permission from Meyer *et al.*, Ultramicroscopy **6**, 67 (1981). Copyright 1981 Elsevier. (d) and (e) show SEM images of charged domain walls in periodically poled $LiNbO_3$. In (d), the negatively charged tail-to-tail walls are visible as black stripes under negative surface charging (3 kV); in (e) positively charged head-to-head domain walls are visible as bright stripes under positive surface charging (1 kV). The SEM data in (d) and (e) are adapted with permission from Aristov *et al.*, Phys. Status Solidi A **86**, 133 (1984). Copyright 1984 John Wiley & Sons, Inc.

In pioneering experiments, the team achieved domain contrast in ferroelectric $BaTiO_3$ using low acceleration voltages. The result is remarkable, as it removed the need for domain-selective-etching for creating topographic features, providing an opportunity to study ferroelectric domains and related phenomena in a much wider range of materials. In the following years, SEM was applied to study different ferroelectrics, including triglycine sulfate (TGS),[70] $Gd_2(MoO_4)_3$,[42] $LiNH_4SO_4$,[71] and $LiNbO_3$[43] [see also Figs. 3(c)–3(e)]. As advances in electron sources, optics and stability greatly improved the low voltage capabilities of SEM, high-resolution imaging became possible giving the SEM the unique ability to image everything from macroscopic ferroelectric and ferroelastic domain structures to nanometer sized domain walls (see Fig. 3).

Originally, however, the primary focus of SEM studies in the field of ferroelectrics was the imaging and characterization of domain structures with little attention being paid to the domain walls. The majority of SEM studies were performed on samples with out-of-plane polarization and neutral domain walls. Charged ferroelectric domain walls were first investigated by SEM in 1984 by Aristov *et al.* in $LiNbO_3$[43] [Figs. 3(d) and 3(e)]. Although the exact contrast mechanism and physical origin of the anomalous response at the domain walls was not known at that time (see Sec. II D), the work already foreshadowed many aspects discussed in modern domain wall research as we will discuss later on.

B. Basic operation

To understand the image formation and emergent domain and domain wall contrasts in SEM, we begin by discussing the basic structure of modern SEMs. A typical SEM consists of (1) the electron source and electron optics column, (2) the specimen chamber with a goniometric stage, and (3) one or more detectors for recording of secondary electrons and backscattered electrons as

© Author(s) 2020

shown in Fig. 4.[67,68,72] In addition, optional optical cameras are available for monitoring the specimen chamber. The electron source is based on thermionic or field emission; the source in the latter case is called a field emission gun (FEG). After the electrons are emitted from the source under a certain acceleration voltage (V), they enter the column where a series of electromagnetic lenses and apertures focuses the beam onto the sample surface. Both the column and the chamber are kept in vacuum ($<10^{-6}$ Pa). Modern SEMs often use an in-lens detector (ILD) where the detector is positioned inside the electron column for immersion mode imaging. The beam diameter, or spot size, is closely tied to the resolution of the microscope and for modern SEMs it can even be sub-nanometer when using a FEG.

As the electrons from the beam (primary electrons, PEs) reach the sample, a variety of complex interactions occurs; for example, the PE can either interact with the negative electron clouds of the atoms or the positive nuclei. The interaction with the nuclei causes the PE to be scattered approximately elastically and, in some cases, electrons are reflected with an energy close to the incident energy (E_0). These reflected electrons are called back-scattered electrons (BSEs). The probability of backscattering increases with atomic number of the material under investigation, which implies that detection of BSEs will contain elemental contrast. Interactions of PEs with the electron cloud of the target atoms are typically inelastic and associated with the generation of secondary electrons (SEs). Generated SEs have a low kinetic energy (<50 eV[73]) and thus quickly recombine with holes so that only SEs generated close to the surface ($\lesssim$30 nm depth) can escape the specimen. SEs can also be generated from BSEs within the material, as well as on surfaces inside the specimen chamber, blurring the imaging results and mixing the SE signal with BSE contrast. The angle of the sample surface with respect to the beam direction, as well as the surface topography, co-determine the region from which SEs can escape, generating topographic contrast which is common when imaging with SEs. Combined with selective etching, such topographic contrast was originally exploited for domain visualization (see Sec. II D 1). Note that the contributing volume of the BSEs, and thus also that of the BSE induced SEs, is highly dependent on the acceleration voltage (V). Thus, lowering the acceleration voltage means the signal is generated from a smaller volume, which can be exploited to increase the resolution. However, V also affects the spot size, with higher V giving the smaller spot size due to reduced aberrations. Thus, a compromise has to be found between probe size and interaction volume to optimize resolution.

To obtain spatially resolved data, the electron beam is raster-scanned across the specimen. At evenly spaced points, the beam stops for a time interval (dwell time) in the range of 1 μs, while the detectors record a SE or BSE signal. The most common detector used is the Everhardt–Thornley detector (ETD); a more detailed explanation can be found elsewhere.[68] The ETD is surrounded by a metallic grid that can be biased positively to attract the low energy SEs for imaging, or negatively to repel them and only detect BSEs instead. Imaging in the immersion mode (immersing the sample in the magnetic field of the objective lens) improves resolution as a smaller probe can be formed but requires the use of a detector mounted in the electron column (ILD). While ETDs can display a so-called shadowing effect due to the positioning on the side of the

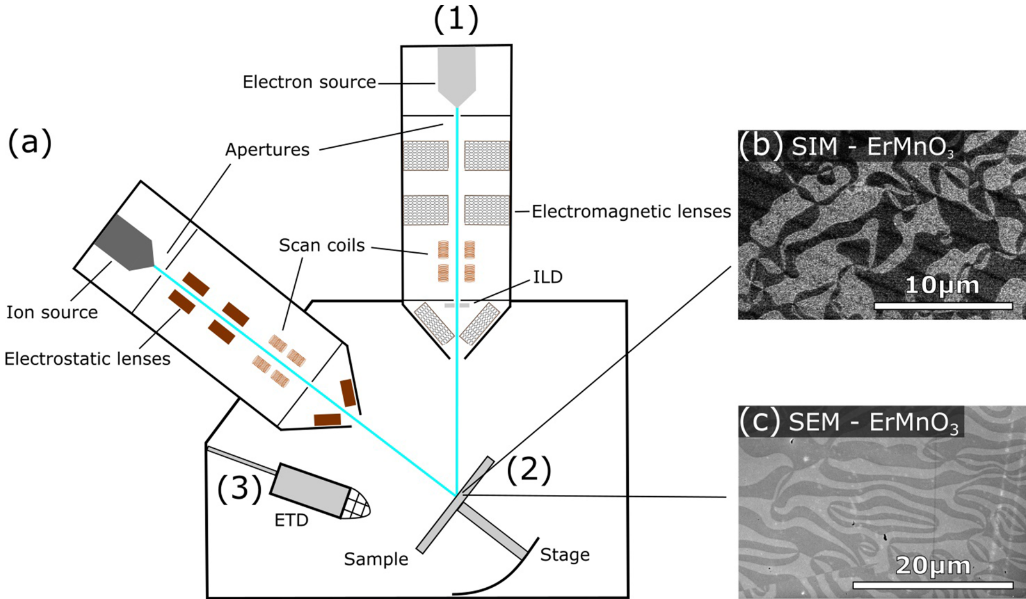

FIG. 4. (a) Schematic of a dual-beam FIB with major components added and labeled. The setup of classical SEMs is similar but without the additional ion beam. (b) Representative example of a domain image gained in SIM mode (SEs generated by ion beams) gained on $ErMnO_3$ with out-of-plane polarization. Bright and dark areas indicate ferroelectric 180° domains with opposite polarization orientation. (c) SEM image recorded on an $ErMnO_3$ sample with the same surface orientation as in (b) with bright and dark areas corresponding to ±P domains.

© Author(s) 2020

chamber, the ILD provides a more homogeneous signal and typically has a better signal to noise ratio. However, even when operating both detectors in the SE imaging mode, there will be a difference in the ratio of BSEs and SEs that reach the detectors because of the geometry and the contrast might differ.[74]

A specific challenge arises for ferroelectric domain and domain wall imaging as ferroelectrics usually exhibit insulating or semi-conducting properties. Thus, irradiation with charged particles can generate a significant surface charge, which affects the imaging conditions. The ratio between emitted electrons and incident electron is called the electron yield (δ). This yield is highly material dependent and varies with the acceleration voltage (V) as sketched in Fig. 5.[69] The figure shows that whenever the yield is not equal to unity, the sample gets charged: for $\delta > 1$ ($V_1 < V < V_2$), the sample charges positively, and for $\delta < 1$ ($V > V_2$ and $V < V_1$), it charges negatively. As a result, the PEs are accelerated or decelerated on the way toward the surface, while the emitted SEs are attracted or repelled from the surface, respectively, dynamically changing the imaging conditions. The charging will proceed until a dynamic equilibrium is reached where $\delta = 1$. For conductive materials such charging can readily be avoided by grounding the sample so that excess charge can dissipate. For ferroelectrics, or insulating materials in general, however, the excess charges accumulate at the surface. This can cause distortions and imaging artefacts. Thus, it is often necessary to adjust and fine-tune the acceleration voltage around $\delta = 1$ to achieve stable imaging conditions. This is particularly challenging when imaging areas with spatially varying conductivity as different areas charge differently, requiring special care.

C. Practical considerations for optimizing domain and domain wall contrasts

1. Acceleration voltage

The acceleration voltage is arguably the most important parameter when imaging ferroelectric domains and domain walls by SEM, becoming increasingly important the more insulating the sample is. The impact on domain and domain wall visualization is well demonstrated in Fig. 6, showing an early example from the seminal work of Le Bihan *et al.*[69] As shown in Fig. 5, for insulating materials, the surface will become positively charged for acceleration voltages between V_1 and V_2, and negatively charged for acceleration voltages higher than V_2 or lower than V_1. For domain contrast, working close to the equilibrium voltage V_1 or V_2 is favorable, because otherwise the deposited surface charge can screen the polarization charges responsible for the contrast. We note that the second equilibrium point V_2 is usually preferred as V_1 is typically so low in energy that aberrations will dominate the final resolution. In contrast, for domain wall imaging off-equilibrium voltages are favorable, because here moderate charging can be useful as discussed in more detail in connection with different models proposed for contrast formation in Sec. II D.

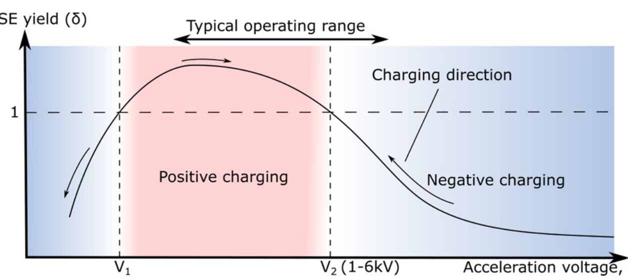

FIG. 5. Schematic of the secondary electron (SE) yield for varying acceleration voltages V.[68] At the equilibrium points, V_1 and V_2, the yield is at unity and there is no surface charging. For $V_1 < V < V_2$, the sample is slightly positively charged, while for $V > V_2$ (and $V < V_1$), the sample becomes negatively charged. When working with voltages $V > V_2$, the dynamical negative charging caused by the electron beam leads to a deceleration of the primary electrons (referred to as charging direction) until V_2 is reached.

In general, strong charging of the material can create pronounced distortions in the SEM images. The distortions usually manifest as large variations in SE emission or drift within a single scan.[75] In principle, finding the equilibrium or optimal voltage is not too difficult. It can be achieved by starting at a low voltage (e.g., 1 kV), progressively increasing the value. If domain or domain wall contrast becomes visible, the voltage can then be fine-tuned until maximum domain/domain wall contrast is reached. In practice, however, dynamical charging effects often occur while imaging, leading to variations in the surface potential and, hence, unstable imaging conditions.

In cases where no contrast is seen from the domains or domain walls after quickly surveying the accessible range of acceleration voltages, or charging is too severe, other basic charging principles may be considered to find the equilibrium voltage where domain contrast is most pronounced. Below V_2, the sample should become positively charged and the scanned area will appear darker than the neutral surface. When the equilibrium point V_2 has been reached, this contrast should invert: the scanned area becomes negatively charged and thus brighter than the neutral surface (see Ref. 68 for more rigorous methods).

2. Secondary parameters (beam current, dwell time, detector, and specimen)

Adjusting the acceleration voltage is not always enough to get good domain and domain wall contrast and even when working at ideal acceleration voltage the contrast can be very subtle, requiring further optimization of secondary parameters. In general, increasing the beam current decreases noise and improves contrasts in SEM, and this also applies for the imaging of domain structures, possibly even more so if the contrast mechanism at play originates either from heating or charging effects (see Sec. II D 1 for details). Note, however, that as the beam current is increased, dynamical charging effects may get more pronounced. In addition, the risk of carbon contamination increases,[76] as well as the risk of poling the ferroelectric sample under the beam while imaging. Both these effects are amplified by using longer dwell times, i.e., slower scans. Faster scanning may be preferred for strongly charging samples, and if excessive charging cannot be avoided, a compromise must be made in terms of beam current and scan speed. In the case of very insulating specimens or multi-component systems, it is helpful to touch a grounded micromanipulator to the sample surface near to

© Author(s) 2020

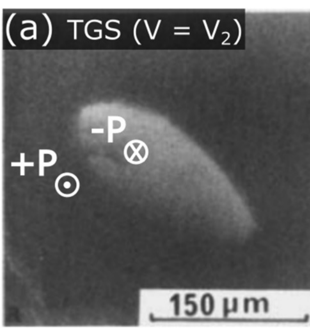

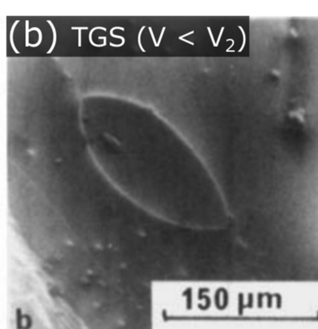

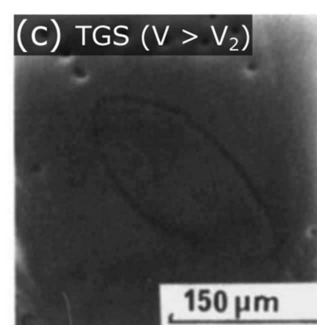

FIG. 6. SEM domain and domain wall images obtained on TGS. The images show how SEM contrast in ferroelectrics with out-of-plane polarization can vary depending on the acceleration voltage V. (a) Domain contrast is achieved for $V = V_2$ with +P domains appearing darker than −P domains (see Fig. 5 for an illustration of the imaging conditions). (b) and (c) show SEM contrast at neutral domain walls gained at $V < V_2$ (bright walls) and $V > V_2$ (dark walls), respectively. Figures are adapted with permission from Le Bihan, Ferroelectrics **97**, 19 (1989). Copyright 1989 Taylor & Francis Ltd.

the region of interest, improving the path to ground. For SEMs without micromanipulators, conductive paint or tape can be placed near the region of interest as an alternative.

Trivially, but very important, clean and flat surfaces with a root mean square roughness in the order of 1 nm, as obtained from proper polishing, eliminate topographic contrast that can dominate over weak domain and domain wall contrast. Finally, it should be noted that both SE[42,69,77] and BSE[78,79] detection modes have been reported to give domain and domain wall contrast, but not necessarily work equally well on the same material. From our experience, the best contrast is achieved using an in-lens detector biased for SE imaging. This can be explained by its high sensitivity to low energy SEs and more effective discrimination of BSE induced SEs thus making it better suited to distinguish between small differences in the SE yield.[74] The discussion in Sec. II D will thus focus on SE detection.

3. Biasing with the electron beam

To verify that SEM contrast originates from ferroelectric domains, the domains may be switched with the electron beam, analogous to PFM studies, where the switching is realized using an electrically biased AFM tip.[70,80,81] If the detected contrast inverts along with the polarization orientation, this is a strong indication that the SEM contrast is of ferroelectric origin. Focusing the electron beam with a high current onto a small region has been demonstrated to create a sufficiently high electric field that can switch the polarization direction.[70,82,83] While the sub-surface domain structure remains unknown, which is a limitation of SEM and surface analysis techniques in general, the surface can be modified with high spatial precision, although one has to be careful not to confuse domain switching with charging effects. As demonstrated, for example, for $LiTaO_3$[80] and $LiNbO_3$,[82,83] the electron beam at higher acceleration voltages (15 kV) induces negative charging at the surface, which can be used to locally flip the polarization from −P to +P. In general, with a small contact-free electron probe any specimen of any geometry can be manipulated and subsequently imaged, reflecting the high flexibility of SEM-based experiments.

D. Contrast mechanisms

1. Out-of-plane polarization

Using SEM, ferroelectric domains and domain walls have been visualized in many ferroelectric materials over the years. Although the technique offers a quick way to image domain structures, a careful analysis is required to make statements about the local ferroelectric properties, because emergent contrast mechanisms can go well beyond the basic description of SE and BSE contrast as observed in common materials as described in Sec. II B.

The original and probably most simple approach for achieving domain contrast is through domain-related topographical variations that arise due to surface treatment, such as chemical polishing and etching processes.[84] In their early work on $BaTiO_3$, Robinson and White exploited that ferroelectric domains with and without surface bound charges etch differently leading to variations in surface roughness, which was used to image 90° domains by SEM [Fig. 3(a)][41] (note that although 90° domains and other variants are common in ferroelectrics, most of the SEM studies have focused on 180° domains). Due to the higher surface roughness and thus larger escape area, the SE yield was found to be enhanced for the positive domains with P normal to the surface so that they are brighter in SEM measurements. Detrimental charging effects were suppressed by depositing a conductive coating onto the sample surface. Alternatively, height differences can also occur, for example, when the domains polish at a different speed, leading to visible domain-related steps in surface topography (i.e., Ref. 41). While this approach allows for studying the domains in out-of-plane polarized specimens, the topography transition from one domain to the next is not necessarily correlated to the existing domain wall structure as walls can, in principle, move after a topographic pattern has been imprinted. Furthermore, *in situ* experiments are not possible and domain switching cannot be captured, and the added conductive layer can limit further investigations with other microscopy techniques, such as conductive or electrostatic force microscopy. Finally, the resolution is limited by the etching/polishing rather than the SEM instrumentation. However, it was later found that using low acceleration voltages, charging can be avoided and a conductive

© Author(s) 2020

coating could be omitted.[85] This discovery was important as it enabled the visualization of domains and domain walls on the polar surface without selective etching.

Aside from topographic contrast, polarization charges and electrostatics associated with the ferroelectric order can be exploited for domain imaging in SEM. Since the first observation of electrostatic contrast variations by Le Bihan in 1972, different theories have been proposed to explain the mechanisms behind SEM domain contrast on polar surfaces.[69,77,86] Three main mechanisms for domain contrast that have been discussed in the literature are illustrated in Figs. 7(a)–7(c), that is, (i) polarization contrast,[69] (ii) pyroelectric contrast,[87] and (iii) emission contrast.[69]

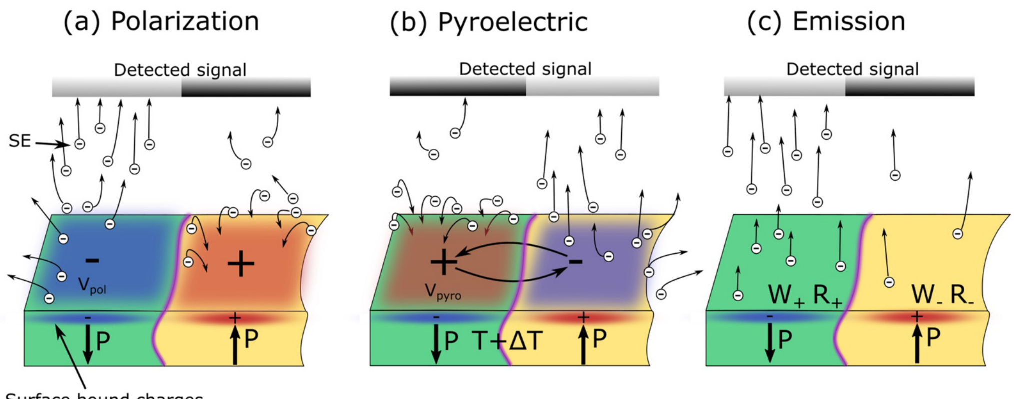

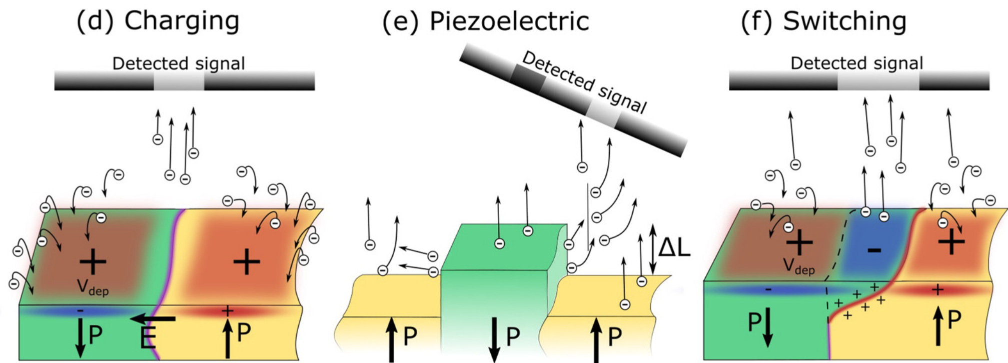

FIG. 7. Main mechanisms that can lead to domain contrast (top row) and domain wall contrast (bottom row) in SEM. (a) Uncompensated negative (blue) and positive (red) bound charges (leading to an electric potential V_{pol}) at the surface of −P and +P domains (− and +) can repel and attract secondary electrons (SEs), respectively. This leads to variations in the SE yield and, hence, the detection of domain contrast, with more intensity for −P domains (light gray) compared to +P domains (dark gray).[69] (b) Due to local heating from the electron beam and the pyroelectric effect, the spontaneous polarization can decrease. Assuming that the bound charges at the surface were initially fully screened, the decrease in polarization can lead to excess screening charges, giving rise to a domain-dependent surface potential (V_{pyro}) that is detectable by SEM. Note that the pyroelectric contrast is inverted compared to the polarization contrast in (a).[87] (c) Physical properties such as work function ($W_{\pm}$) and penetration depth ($R_{\pm}$) can be different from one domain to another leading to changes in SE emission and, in turn, to domain contrast.[69] (d) Because of the bound charges at the surface of −P and +P domains, a built-in electric field E exists (in-plane), where the domain wall intersects with the sample surface. This built-in field forces PEs and SEs into adjacent domains, keeping the wall neutral. Under positive surface charging, a potential V_{dep} arises. The wall region which has remained less charged than the bulk will have a smaller attraction of SEs and more detected yield.[69] (e) Deposited charge and the accompanying converse piezoelectric effect cause contraction and expansion of domains leading to a change in topography. When using a side-mounted detector (ETD), half the domain walls will have a larger exposed surface and the detector will detect more SEs.[87] (f) Due to local beam-induced switching, domain walls can tilt away from their ideal charge-neutral position. Under positive charging, −P domains expand and domain walls can tilt as sketched in (f), changing the domain wall configuration and the local surface charge state. Assuming that surface charges in the switched area are not instantaneously screened, the emergent negative surface bound charges in the inverted area will create a negative surface potential relative to the screened regions, which increases the SE yield.[77] In addition, the emergent domain wall bound charges and related changes in local conductivity can result in SEM contrast (see Fig. 8).

© Author(s) 2020

Mechanism (i) was discussed in connection with $BaTiO_3$, where the domain contrast has been attributed to uncompensated surface bound charges that arise from the bulk polarization [Fig. 7(a)]. The bound charges either repel or attract the SEs, reducing the yield for domains with positive surface charges compared to domains with negative surface charges. This effect was also used to explain the domain contrast observed in TGS [Fig. 6(a)], where domains with positive surface charges appeared to be darker than the domains with negative surface charges. While it is clear that a surface potential will alter the SE yield, the origin of the surface potential is not always clear and much more difficult to determine. This is because surface bound charges can be screened to a varying degree by free charge carriers (ionic or electronic); this charging may further vary dynamically while imaging, and the contribution and impact of potentially charged adsorbents on the surface are often unknown. The potential impact of adsorbents is reflected, e.g., by x-ray photoemission electron microscopy (X-PEEM), low-energy electron microscopy (LEEM), and x-ray photoelectron spectroscopy (XPS) studies,[88,89] and analogous systematic investigations on ferroelectric domains and domain walls by SEM are desirable.

Aside from polarization contrast, the pyroelectric effect can lead to domain contrast in SEM as a result of heating by the electron beam.[87] A pyroelectric potential is formed as the polarization value changes due to the heating with opposite value for opposite domains [Fig. 7(b)], given that emergent changes $\Delta P = P(T) - P(T + \Delta T)$ are not screened instantaneously. The resulting domain-dependent surface potential modifies the total number of SEs reaching the detector in a similar way as in the model considering polarization charges at a constant temperature. As a consequence, different equilibrium voltages V_2 exist for the two domain states (see Fig. 5). It is important to note that the domain contrast evolving from the pyroelectric effect [Fig. 7(b)] is inverted compared to the contrast that arises from surface bound charges [Fig. 7(a)], highlighting the importance of a careful analysis to identify the correct polarization orientation and mechanism at play. Furthermore, variations in other physical properties can cause or contribute to the domain contrast, such as differences in electron penetration depth ($R_{\pm}$) and work function ($W_{\pm}$) [Fig. 7(c)].

Compared to the phenomena observed for 180° domains with out-of-plane polarization we discussed so far [Figs. 7(a)–7(c)], the interpretation of effects related to the associated neutral domain walls is even more challenging. This is because the domain walls can have completely different intrinsic properties than the bulk (see Sec. I A), leading to a different interaction with the PEs and SEs. In particular, their electronic and thermal conductivity can be different, which is known to be crucial for the contrast formation in SEM. However, while it is clear that this correlation enables new research opportunities, systematic, and comprehensive SEM-based investigations of local transport phenomena at ferroelectric domain walls remain to be realized.

An early model from Le Bihan[69] (charging contrast model) explained the contrast at neutral 180° domain walls in out-of-plane polarized samples based on a built-in electric field. The built-in electric field arises from the bound surface charge next to the wall, pushing the PEs into the adjacent domains so that the neutral walls do not charge up as shown in Fig. 7(d). Thus, the yield for the walls will be higher than for the bulk when the surface is positively charged, owing to less attraction of SEs, and lower than for the bulk when the surface is negatively charged [see also Figs. 6(b) and 6(c)]. Similar effects are also expected if the neutral domain wall exhibits a higher conductivity than the domains, which locally reduces the charging under the electron beam. This becomes increasingly important for thinner samples and films grown on conducting back-electrodes, where it becomes more likely that conducting domain walls directly connect surface to ground, leading to substantially reduced resistivity relative to the domains. A second model (piezoelectric contrast) is presented in Fig. 7(e), where domain wall contrast is attributed to topographical variations caused by the *converse* piezoelectric effect: as the sample charges, a surface potential builds up, which leads to a contraction or expansion of the ferroelectric domains, depending on the acceleration voltage and the respective polarization orientation. The latter translates into domain dependent variations in surface topography, which can be resolved in SEM [Fig. 7(e)]. When using a side-mounted detector (ETD), half of the domain walls will have a larger exposed surface and the detector will detect more SEs so that these walls appear brighter in SEM.[87] Alternatively, SEM contrast can arise as domain walls are bent away from their ideal charge-neutral configuration (switching contrast) due to local heating or surface charging by the electron beam.[77,86] When negative domains expand, as it is the case for positive surface charging, the switched area will develop a negative surface potential, assuming that the bound charges of the newly switched area are not screened instantaneously. The surface potential then deaccelerates PEs and repels SEs, increasing the yield so that the switched area appears brighter [Fig. 7(f)]. Aside from the emergent surface potential due to domain switching, the domain walls bend away from their charge-neutral position, which leads to domain wall bound charges. The latter can cause additional contrast contributions as explained in detail in Sec. II D 2, where we address SEM imaging of charged domain walls.

The overview presented in Figs. 7(d)–7(f) shows that the interpretation of domain wall contrast in SEM can be highly nontrivial and the exact mechanisms are still far from being fully understood. The development of a more comprehensive model explaining the SEM contrast formation at nominally neutral ferroelectric domain walls is therefore highly desirable to enable quantitative measurements and benefit from the SEM`s nanometer spatial resolution and high sensitivity to electronic and electrostatic domain wall properties.

2. In-plane polarization

Compared to surfaces with out-of-plane polarization, surfaces where the polarization lies in-plane are far less studied with SEM. Domain contrast has been observed on surfaces with in-plane polarization,[43] and the contrast has been explained by the emission model [Fig. 7(c)], assuming that oppositely polarized domains have a difference in emission at equilibrium conditions. However, additional work is desirable to clarify the origin of ferroelectric domain contrast in SEM on non-polar surfaces. Importantly, it was clear early on that emergent domain wall contrasts can provide valuable information about the physical properties at charged ferroelectric domain walls. In addition to the phenomena that arise at neutral

© Author(s) 2020

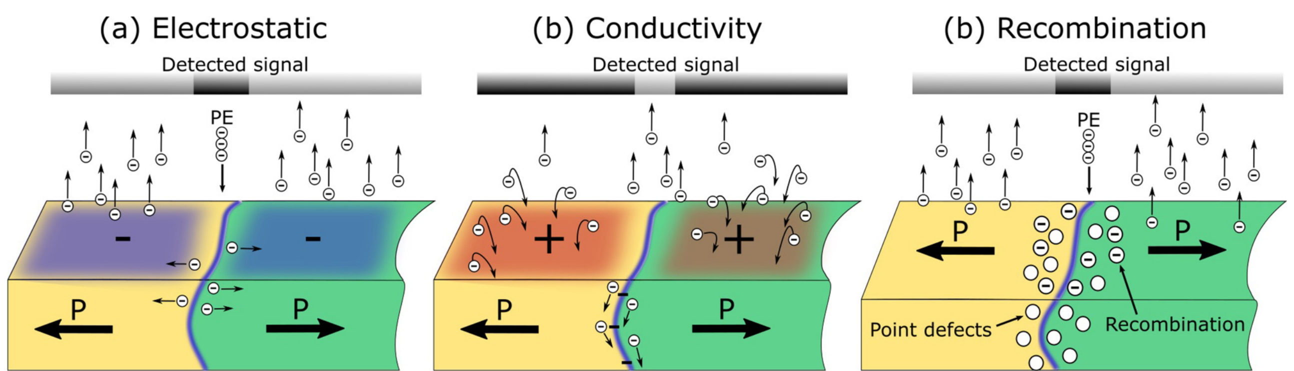

FIG. 8. SEM contrast at charged domain walls. (a) Under negative surface charging, the potential barrier at a negative tail-to-tail domain wall prevents negative charges to accumulate, keeping it more neutral with less yield (same as in Fig. 6). (b) Enhanced conductivity at domain walls can locally reduce charging effects,[32] causing a potential difference relative to the more insulating domains. Analogous to (a), this potential difference influences the SE yield, leading to domain wall contrast in SEM. (c) Recombination contrast illustrated for the case of a negatively charged tail-to-tail domain wall (blue line). One possibility to screen the negatively bound charges at tail-to-tail domain walls is to accumulate positively charged ionic defects (white circles). It has been proposed that such ionic defects may locally increase the recombination activity for the primary electrons (PE), which reduces the SE yield at the position of the domain wall so that they are darker than the in-plane polarized domains in the SEM image.

walls, the charged domain walls exhibit bound charges and diverging electrostatic potentials that add to their complexity, as well as pronounced variations in electronic conductivity.

The first observation of charged domain walls by SEM was made in 1984 by Aristov *et al.*[43] By mapping the ferroelectric domain structure in $LiNbO_3$ under negative charging conditions (Fig. 5), it was found that tail-to-tail domain walls became visible due to a lower SE yield than the bulk [Fig. 3(d)]. For positive surface charging, the positively charged head-to-head domain walls became visible because of a higher SE yield than the bulk [Fig. 3(e)]. The authors explained this effect based on electrostatics, arguing that the domain wall represents a potential barrier which prevents charges to accumulate. For instance, under negative surface charging [Fig. 8(a)] a negative domain wall (tail-to-tail) would be kept neutral and thus exhibit a lower yield than the bulk due to less repulsion of SEs and PEs. The opposite happens at the head-to-head walls, which remain neutral under positive charging so that more SEs reach the detector. Alternatively, differences in the surface potential can arise at charged domain walls due to their distinct electronic transport properties [conductivity contrast, Fig. 8(b)]. X-ray photoemission electron microscopy (X-PEEM) measurements demonstrated that surface charging is suppressed at charged domain walls with enhanced conductivity.[32] The correlation between domain wall conductivity and SEM contrast is evident from recent measurements on $ErMnO_3$, revealing a direct connection between SEM domain wall contrast and the local transport properties[90] [see Figs. 9(b)–9(d)].

In 2007,[91] further investigations on poled $LiNbO_3$ with charged domain walls showed that the SE yield at negative tail-to-tail domain walls is higher than for the bulk under positive surface charging and lower under negative surface charging (head-to-head domain walls were not reported). It was suggested that the SEM contrast could be due to increased recombination activities, resulting from an accumulation of point defects and impurities at the negatively charged domain walls. This could reduce the negative charging at the wall and thus lead to a lower yield [Fig. 8(c)]. Although the results are not fully consistent with the aforementioned SEM study on charged domain walls in $LiNbO_3$,[43] the work is intriguing as it foreshadows the possibility to apply SEM to explore the local defect chemistry at charged ferroelectric domain walls.[92] In general, it is very likely that multiple effects are present, contributing simultaneously to the SEM contrast at charged domain walls. Thus, especially with fixed imaging conditions, it is challenging to unambiguously identify the physical origin of the contrast as reflected by the work on charged domain walls in $LiNbO_3$.

In conclusion, although SEM attracted much attention for imaging ferroelectrics early on, the reported observations have shown that we still do not have a good enough understanding of the underlying contrast mechanisms. In this sense, it is an overlooked technique with more potential, considering its great flexibility and speed in visualizing both nanoscale and macroscopic domain structures. However, it is also clear that a better understanding of the contrast formation process and the development of a comprehensive theory is highly desirable to deconvolute competing contrast-formation mechanisms and ultimately facilitate quantitative SEM-based measurements at domain walls in ferroelectrics.

III. DUAL-BEAM FOCUSED ION BEAM

Seen as a surface analysis technique for ferroelectric domains and domain walls, SEM combines several key aspects, offering non-destructive and contact-free imaging with high spatial resolution. Furthermore, SEM is much faster than comparable domain analysis techniques such as PFM. Possibly the biggest advantage of SEM is the opportunity to combine domain wall imaging with other nano-characterization and fabrication tools. Most notably, the dual-beam FIB (focused ion beam, Fig. 4) combines nano-structuring with

© Author(s) 2020

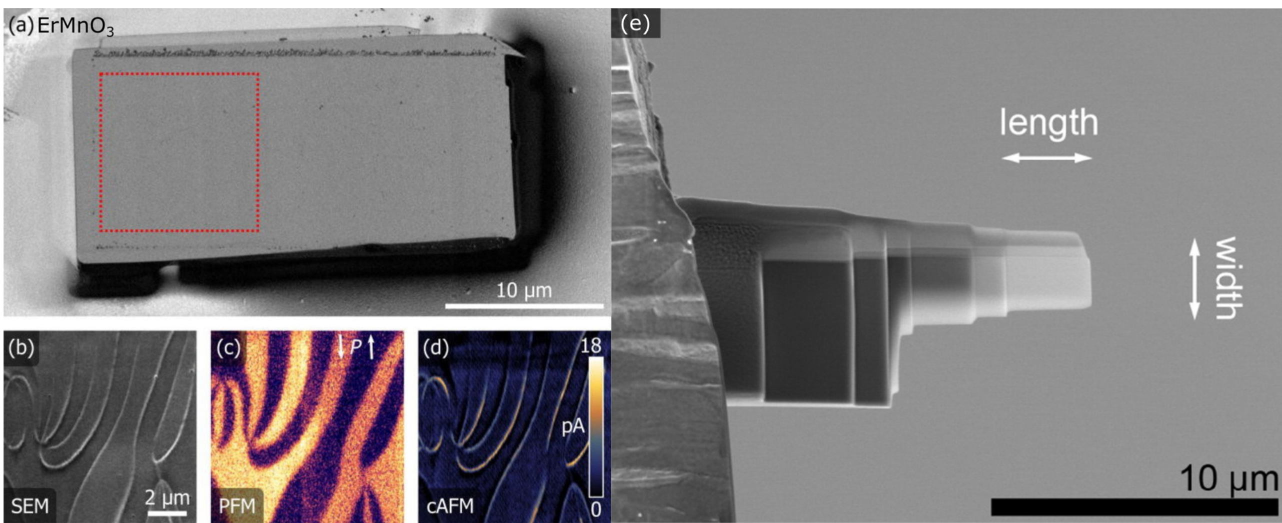

FIG. 9. Applications of dual-beam FIB to ferroelectrics. (a) SEM image (BSE mode) of an $ErMnO_3$ lamella with in-plane polarization, extracted from a bulk sample using a dual-beam FIB.[90] The red dashed square marks the region where the data shown in (b)–(d) was recorded. (b) SEM image (SE mode) obtained in the area marked in (a). Ferroelectric domain walls are visible as bright lines on a homogeneous gray background. (c) PFM image (in-plane contrast) of the same location as in (b), revealing the polarization direction in the domains (bright: −P; dark: +P). (d) cAFM data showing enhanced conductance at the position of the domain walls. Consistent with Ref. 17, tail-to-tail domain walls are observed to exhibit higher conductance than the head-to-head domain walls, reproducing the contrast levels observed in the SEM scan in (b). (a)–(d) are reproduced with permission from Mosberg *et al.*, Appl. Phys. Lett. **115**, 122901 (2019). Copyright 2019 AIP Publishing LLC. (e) Example of a TEM lamella prepared by FIB. The lamella is attached to a half TEM grid (left side) in a "flagpole" geometry, where the outermost part of the lamella has a thickness below 40 nm.[100] Image is adapted with permission from Schaffer *et al.*, Ultramicroscopy **114**, 62 (2012). Copyright 2012 Elsevier.

high-resolution imaging within one setup, enabling preparation of ferroelectric specimens with varying shapes and dimensions for domain engineering,[93–96] as well as correlated microscopy studies of domain walls in device-relevant geometries.[97] Here, we will focus on these two topics and give recent examples related to domain wall research. For a comprehensive introduction to the FIB, we refer the reader to, e.g., the textbook by Yao.[95]

A. Ions vs electrons

The basic setup of FIB optics is very similar to the SEM optics (Fig. 4), but instead of an electron beam, FIB uses an ion beam.[95] Replacing the electron source by a liquid-metal ion source, typically Ga^+, results in completely new functionality. In general, FIB has four basic applications: milling, deposition, implantation, and imaging. In addition, supplementary features, such as micromanipulators, energy dispersive x-ray spectroscopy (EDX) and compatible probe stations are often found on FIB instruments, making it a highly useful toolkit for nanotechnology-related research. Originally, the FIB was developed for the semiconductor industry to do microfabrication and failure analysis, but today it is also extensively used in research laboratories for characterization and specimen preparation at nano- to macroscopic length scales.

Many modern FIBs include an SEM, referred to as *dual-beam* FIB. Here, both microscopes use the same vacuum chamber and detector system, and the two beams (electrons and Ga^+) are coincident at the sample surface (Fig. 4). In contrast to the electron beam, the ion beam is focused with electrostatic lenses (not electromagnetic) due to the higher ion mass compared to an electron. When reaching the sample, the heavy Ga^+ ions strongly interact with the surface atoms. This interaction can be an elastic collision with the nucleus and/or inelastic processes with the electron cloud generating SEs. Due to the large mass of the incident ion, the former interaction can transfer significant momentum to the target atoms, knocking them out of position. This creates a cascade of collisions in the targeted specimen and can lead to sputtering of surface atoms, which is the basis for ion beam milling. Aside from milling, the incident Ga^+ beam can cause amorphization and implantation of Ga^+. Related artefacts can be minimized by adequately adjusting the acceleration voltage of the Ga^+ beam. Lower acceleration voltages typically lead to more implantation, but also a smaller penetration depth and thinner damage layers. Should the sputtered atoms also be ionized and emitted from the surface as SI (secondary ions), they can be detected and reveal strong elemental contrast. Due to ion channeling, the penetration depth of the Ga^+ ions depends on the crystal orientation. The likelihood for SEs to escape and be detected increases and thus contrast due to variations in crystallographic orientation is possible for ion induced SE imaging.

In general, the FIB retains the basic imaging functions, complementary to the electron imaging of the SEM, referred to as scanning ion microscopy (SIM, see Fig. 4). The biggest advantage, however, arises from the added functionalities beyond just imaging. For instance, sputtering can be used to remove the surface layer-by-layer and create cross sections of the material to reveal sub-surface structures. Furthermore, by introducing gases into the

© Author(s) 2020

specimen chamber, the ion beam can be used for depositing electrical surface contacts or protecting capping layers with nanoscale spatial precision. Typically, this would be tungsten or platinum when high conduction is required, or carbon and silicon dioxide for a more resistive material. Please note that the deposits contain high amounts of carbon remains for the carrier molecules and Ga with ion-assisted deposition.[98,99] Combining the different deposition possibilities with milling allows for complete 3D nanostructuring. Another essential feature of modern FIBs are integrated micromanipulators, which allow for extracting specimens with the desired shape and dimension from bulk samples. Other micromanipulator setups include probe stations that enable *in situ* characterization of local transport properties, making the FIB a well-equipped toolbox for studying ferroelectric domain walls. In the following, we will give two examples that highlight how the application of dual-beam FIB pushes the frontiers of domain wall research, addressing the extraction and study of individual domain walls (Fig. 9) and creation, and testing of device-relevant geometries (Fig. 10).

B. Specimen preparation and nanostructuring

FIB-SEM is widely used to prepare specimen for the TEM,[93,100] which otherwise can be a time-consuming process and less site-specific. The FIB can readily extract lamellas (typical dimensions: 5 to 10 μm squared and 1 μm thick) from a site-specific region of interest (ROI) with 10 nm precision and thin the lamella down to the desired thickness and shape [Fig. 9(e)]. As a result, the FIB has become a standard tool for TEM specimen preparation. The preparation of thin lamella-shaped specimen, however, is no longer just of interest to enable high-resolution TEM studies. Nanostructuring by FIB-SEM has evolved into a research field by itself, enabling preparation and manipulation of materials to study confinement effects, emergent phenomena at the nanoscale and more.[97] For example, FIB-SEM has been used to tailor ferroelectrics leading to different breakthroughs, including the creation of exotic domain states and controlled injection of domain walls with nanoscale spatial precision.[96,101]

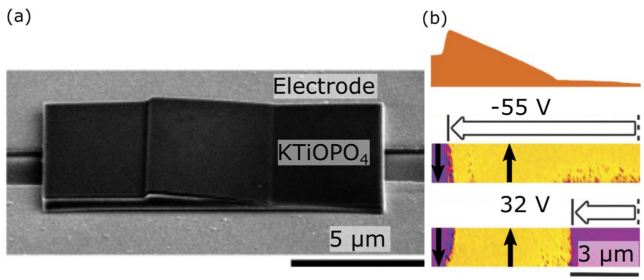

FIG. 10. FIB-SEM nano-structuring of ferroelectric devices. (a) SEM image of a ferroelectric domain wall diode. (b) In the top, a schematic of the topography is shown and below are two PFM images taken after a voltage pulse has been applied to the lamella in single domain state. First, a voltage pulse of −55 V is applied, creating a domain wall that is moved from the right to the left, stopping at the surface step. Then, a second voltage pulse of +32 V is applied, creating a new domain wall and moving it to the base of the wedge. Dark arrows in the PFM image indicate the polarization direction, and bright arrows indicate domain wall movement. Adapted with permission from Whyte and Gregg, Nat. Commun. **6**, 7361 (2015). Copyright 2015 Springer Nature.

As we discussed in Sec. I, conductive domain walls have been intensively studied and great progress has been made in recent years. Yet, the investigations mostly focused on the application of surface sensitive techniques, while more detailed information on the 3D structure is needed for a better understanding of the unusual electronic transport phenomena at ferroelectric domain walls. Using FIB-SEM, it becomes possible to study individual domain walls with a well-defined geometry as recently demonstrated by measurements on the hexagonal manganite $ErMnO_3$.[90] Using a micromanipulator, a lamella was extracted from a bulk out-of-plane polarized sample. After extraction, the lamella was further thinned down to 700 nm and then polished with the ion beam at low acceleration voltages to remove the surface damage layer and improve contrast of surface sensitive techniques. This approach made it possible to image the lamella from both sides in SEM, giving an estimate of the orientation of the domain walls in 3D via linear extrapolation. The lamella was then placed on an MgO substrate for correlated PFM and cAFM studies as shown in Figs. 9(b)–9(d). The correlated investigations, combined with the knowledge about the 3D structure, enabled a refined understanding of the conducting domain walls. In particular, the work explained why deviations from the expected transport behavior occur when considering only the domain wall state at the surface, highlighting the importance of the domain wall orientation hidden within the bulk.

Going beyond the advanced imaging capabilities, 3D nanostructuring by FIB has been applied to control domain wall motions exploiting size-effects. Although ferroelectric domains can be controlled with electric fields, they will only shrink and expand depending on the direction of the electric field. Domain walls enclosing one domain will then necessarily move in opposite directions. In order to achieve a unidirectional movement, the surface of the ferroelectric material can be altered, creating an asymmetric potential landscape for the domain walls, facilitating the design of domain-wall based shift registers as demonstrated by Whyte *et al.*[102]

Figure 10 shows a domain wall diode extracted from ferroelectric $KTiOPO_4$ using FIB, representing an intriguing example for 3D nanostructuring. A lamella was extracted from a bulk sample and placed between two electrodes as shown in Fig. 10(a). While the backside was kept flat, the surface of the lamella was milled into a wedge shape followed by a step in the topography, as sketched in Fig. 10(b). Ga^+-induced damage at the surface was partially removed by thermal annealing and subsequent acid etching.[103] A strong electric pulse of +100 V was then applied to remove any existing domains, followed by two electric pulses of −55 V and +32 V, respectively. PFM images were acquired after each pulse as shown in Fig. 10(b), where the domain walls are the interfaces between up (yellow) and down (purple) polarized domains. The first pulse nucleated a domain in the right part of the lamella, which progressively moved to the left and over the surface step. During the second pulse, the surface step prevents the existing domain wall from moving to the right and instead a second domain wall was nucleated and moved toward the left. Thus, the

© Author(s) 2020

domain walls can only move in one specific direction, analogously to the operating principle of a conventional diode that only allows current to flow from the anode to cathode.

In conclusion, the examples in Figs. 9 and 10 reflect the diverse application opportunities of combining FIB nanostructuring and SEM imaging in the field of domain wall nanoelectronics. Applications range from the characterization of the transport behavior at individual domain walls to the creation of device-relevant geometries that allow for precise control of domain wall motions. At present, however, we are just beginning to explore all the different nanofabrication capabilities and related opportunities for the research on functional domain walls. We anticipate that FIB-SEM will play an important role in the future for facilitating proof-of-concept devices such as memory cells, domain wall enabled memristors, and FE-RAM with domain-wall based read-out.

IV. CORRELATED SEM AND ATOM PROBE TOMOGRAPHY INVESTIGATIONS OF INTERFACES

In this last part of the Tutorial, we will go beyond conventional and rather well-established research directions and discuss possible future opportunities for the studies of ferroelectric domain walls, arising from the combination of FIB-SEM and atom probe tomography (APT). We consider this combination a particularly promising example as it allows for characterizing domain walls in 3D down to the atomic scale and with highly sensitive element-specific compositional analysis.[104–108] This capability facilitates unprecedented insight into the chemical composition of domain walls and their interaction with point defects, which may lead to important breakthroughs in the field of domain wall nanoelectronics, likely pushing the state of the art in the years to come.

A. Atom probe tomography

The basic function of an APT instrument is to field evaporate materials atom-by-atom, which are then detected using a time-of-flight method so that the atoms can be identified (i.e., chemically labelled) and back projected onto a virtual specimen to build a 3D model. For details about the setup and the general working principle of APT we refer the reader to, for example, the textbook by Gault *et al.*[106] Here, we will restrict ourselves to a short summary of key parameters, focusing on the added value of combined FIB-SEM and APT for the study of ferroelectric domain walls.

To evaporate atoms, ideally "one at a time", a strong electric field is needed ($\sim 10^{10}\,\mathrm{V\,m^{-1}}$), which is achieved by the combination of a positive high voltage source, between 2 and 12 kV, and a specific shape of the sample under investigation: in APT, the sample usually has the shape of a sharp needle with tip radius of 50 to 150 nm. By measuring the (x, y)-coordinates for each atom at a given position, i.e., the position of the 2D detector (microchannel plate and delay-lines), the original position of the atom on the specimen surface before evaporation can be deduced considering its trajectory in the applied electrostatic field. The third coordinate is then calculated based on the tip geometry and the ionic volume resulting in a full 3D measurement of the atomic positions. To also obtain the time-of-flight, which is directly related to the mass-to-charge ratio of the detected atom/ion, laser pulses (or voltage pulses) are applied to the specimen tip, which controls the time of departure, making the APT method element specific. In modern APT instruments, up to 80% of the evaporated atoms are detected and for every single atom the mass-to-charge ratio can be determined. Studying materials in this atom-by-atom fashion results in outstanding chemical sensitivity which, combined with the sub-nanometer spatial resolution, puts APT in a unique position for 3D nanoscale investigations.[109,110]

Originally relying on voltage pulsing, the application of APT used to be restricted to metals, shaped into needles by electropolishing. Because of this, the technique has been applied extensively to metals for studying the composition of precipitates, dislocations, and grain boundaries.[104,111] Today, with the integration of the laser-based evaporation and sample preparation by dual-beam FIB, virtually any material can be investigated, opening the door for APT studies of ferroelectric domain walls. However, due to the small analysis volumes (in the range of $10^7\,\mathrm{nm}^3$), careful preparation of specimens is key for a successful APT analysis of domain walls.[112–115] Here, SEM and its capability to image ferroelectric domain walls comes into play (see Sec. II), with FIB allowing extraction of individual walls with nanoscale spatial precision. As an example of the potential of combined FIB-SEM and APT studies, we briefly discuss the recent work by Xu *et al.*[118] on grain boundaries in oxides in Sec. IV B.

B. Applications of APT to interfaces in oxides

Analogous to ferroelectric domain walls, it is established that grain boundaries in ionic conductors can exhibit enhanced or reduced conductivity,[116] representing quasi-2D systems with specific properties different from the homogenous bulk. The origin of the anomalous transport behavior at the boundaries is often attributed to impurity elements accumulating at the grain boundary.[117]

Figure 11 presents an APT study of a grain boundary in Sm-doped CeO_2 from the recent work by Xu *et al.*[118] In Fig. 11(a), a SEM image is shown of the needle specimen before and after the APT analysis. This specimen was extracted from the specific location of a grain boundary, which was identified with the SEM. The corresponding APT analysis is presented in Fig. 11(b), which shows that Sm is homogeneously distributed in the bulk, with additional impurity elements that are nominally only a few ppm accumulated at the boundary. As the APT technique has a sensitivity as low as a few ppm, it can readily detect such small concentrations well below 0.1 at. %, in addition to their spatial distribution around the grain boundary.

The impurity elements where shown to cause a space charge potential at the grain boundary, leading to a depletion of oxygen vacancies. Similar findings have previously been made on doped $SrTiO_3$,[117,119] where grain boundaries of doped samples show a negative potential at the grain boundary core, in contrast to pristine samples that showed no sign of such electrostatic potential. This combination of SEM and APT led to a breakthrough in understanding the origin of grain boundary transport properties, and the same procedure could be applied to study the impact of point defects at domain walls, leading to novel insight regarding the nanoscale physics and defect chemistry at functional domain walls in ferroelectrics.

© Author(s) 2020

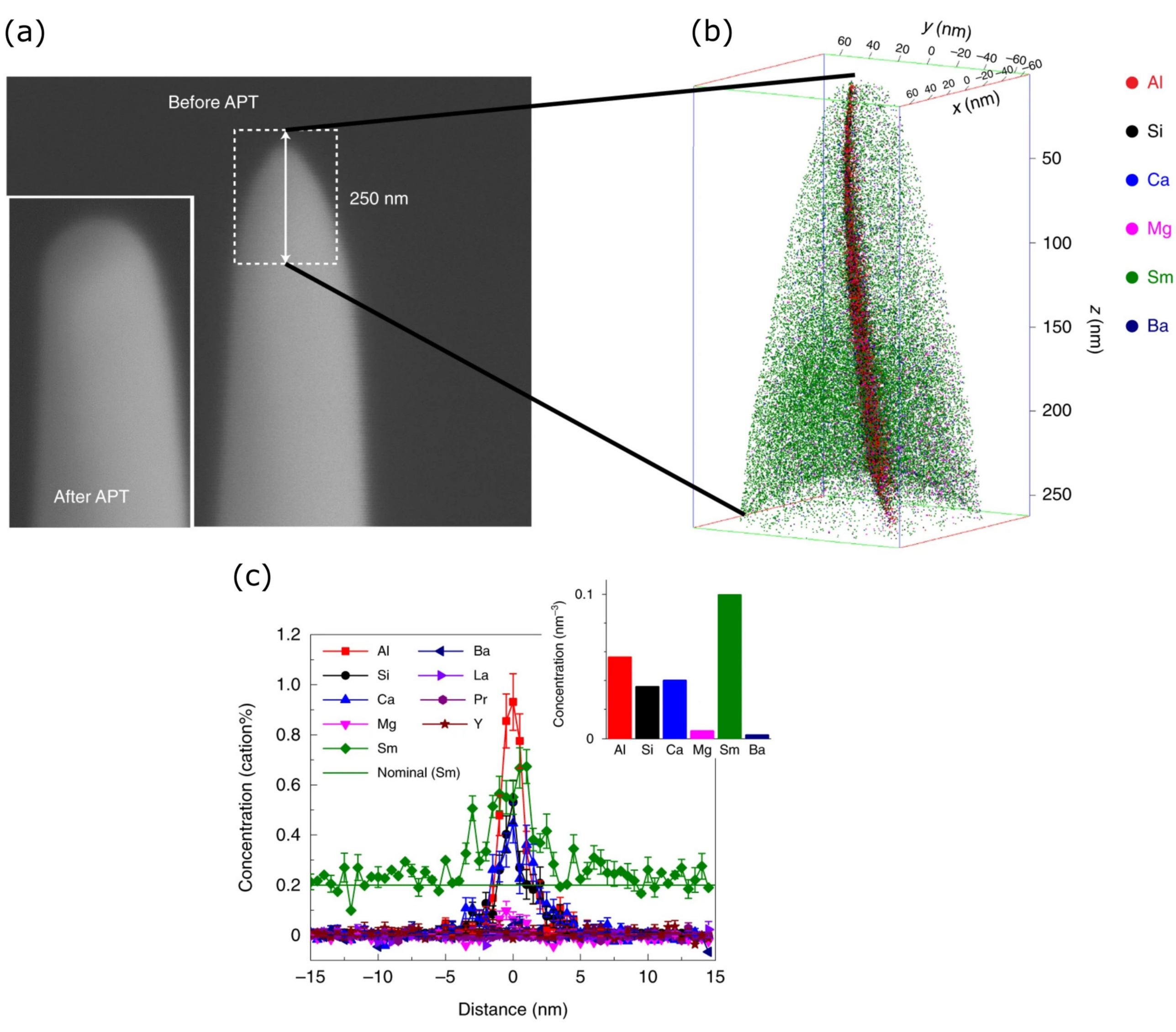

FIG. 11. Combining SEM and APT. (a) SEM image of a needle-shaped Sm-doped CeO_2 sample, obtained before and after (inset) APT analysis. The SEM data shows how the needle is blunted during the APT analysis, resulting from successive field evaporation of the surface atoms. (b) 3D reconstruction of the evaporated area of the needle in (a). Here, only the impurity ions are shown. The Sm atoms are homogeneously distributed within the specimen. In contrast, at the grain boundary located in the center of the needle, an accumulation of various other elements is observed. (c) Cross-sectional data showing the variation in concentration for different elements across the grain boundary in (b). Adapted with permission from Xu *et al.*, Nat. Mater. **19**, 887 (2020). Copyright 2020 Springer Nature.

V. CONCLUSION

For about half a century, scanning electron microscopy (SEM) has been used to visualize the domain and domain wall distribution in ferroelectrics, providing a unique opportunity for scale-bridging microscopy studies and continuously covering nano- to mesoscopic length scales. In addition, the SEM measurement is contract-free and fast, with typical data acquisition times in the order of a few seconds. On the one hand, it is an advantage of SEM that diverse mechanisms can be exploited to achieve domain and domain wall contrast, making it applicable to a wide range of ferroelectric materials. On the other hand, this diversity of contrast mechanisms often makes it difficult to identify the dominant contribution, making the data analysis at ferroelectric domain walls highly nontrivial. At this point, we do not understand the contrast formation well enough, which is reflected by the patchwork-like selection of models that have been proposed to explain observed SEM contrast at neutral and charged domain walls. The development of a comprehensive theory for the contrast formation at ferroelectric

© Author(s) 2020

domain walls is highly desirable in order to achieve quantitative insight and fully exploit the benefits offered by SEM.

The perhaps biggest advantage of SEM is its outstanding flexibility when it comes to correlated studies beyond just imaging. Dual-beam FIB-SEM allows for combining imaging with nanostructuring, correlated microscopy measurements, and *in situ* switching experiments. In addition, *in operando* studies are feasible, allowing to study the performance of domain walls in devices and device-relevant geometries.

Other opportunities that are yet to be explored fully are combinations with advanced characterization methods such as atom probe tomography (APT), enabling 3D chemical structure analysis at domain walls with unprecedented precision. In addition, the option to both image and cut in FIB-SEM instruments can be used to resolve domain wall structures in 3D and with nanoscale spatial accuracy; setups with micromanipulators are further capable of four-probe transport measurements, providing a pathway to determine the intrinsic conductivity at domain walls.

In summary, SEM has shown its value and still has a huge potential for studying ferroelectric domain walls that is yet to be unlocked, and with the field moving closer and closer to first device applications, it is likely that *in situ/in operando* studies by SEM will play an increasingly important role in the future.

DATA AVAILABILITY

The data that support the findings of this study are available within the article.

ACKNOWLEDGMENTS

D.M. acknowledges support by NTNU through the Onsager Fellowship Program and the Outstanding Academic Fellows Program, and funding from the European Research Council (ERC) under the European Union's Horizon 2020 Research and Innovation Programme (Grant Agreement No. 863691). The Research Council of Norway is acknowledged for support to the Norwegian Micro- and Nano-Fabrication Facility, NorFab (Project No. 295864).

REFERENCES

[1]J. Valasek, Phys. Rev. **17**, 475 (1921).
[2]M. E. Lines and A. M. Glass, *Principles and Applications of Ferroelectrics and Related Materials* (OUP, 2001).
[3]S.-W. Cheong and M. Mostovoy, Nat. Mater. **6**, 13 (2007).
[4]T. Kimura, T. Goto, H. Shintani, K. Ishizaka, T. Arima, and Y. Tokura, Nature **426**, 55 (2003).
[5]A. K. Yadav, C. T. Nelson, S. L. Hsu, Z. Hong, J. D. Clarkson, C. M. Schlepütz, A. R. Damodaran, P. Shafer, E. Arenholz, L. R. Dedon, D. Chen, A. Vishwanath, A. M. Minor, L. Q. Chen, J. F. Scott, L. W. Martin, and R. Ramesh, Nature **530**, 198 (2016).
[6]F.-T. Huang and S.-W. Cheong, Nat. Rev. Mater. **2**, 17004 (2017).
[7]S. Das, Y. L. Tang, Z. Hong, M. A. P. Gonçalves, M. R. McCarter, C. Klewe, K. X. Nguyen, F. Gómez-Ortiz, P. Shafer, E. Arenholz, V. A. Stoica, S. L. Hsu, B. Wang, C. Ophus, J. F. Liu, C. T. Nelson, S. Saremi, B. Prasad, A. B. Mei, D. G. Schlom, J. Íñiguez, P. García-Fernández, D. A. Muller, L. Q. Chen, J. Junquera, L. W. Martin, and R. Ramesh, Nature **568**, 368 (2019).
[8]E. Salje and H. Zhang, Phase Transit. **82**, 452 (2009).
[9]G. Catalan, J. Seidel, R. Ramesh, and J. F. Scott, Rev. Mod. Phys. **84**, 119 (2012).
[10]D. Meier, J. Phys. Condens. Matter **27**, 463003 (2015).
[11]D. Meier, J. Seidel, M. Gregg, and R. Ramesh, *Domain Walls—From Fundamental Properties to Nanotechnology Concepts* (Oxford University Press, 2020).
[12]D. M. Evans, V. Garcia, D. Meier, and M. Bibes, Phys. Sci. Rev. **5**, 20190067 (2020).
[13]C.-L. Jia, S.-B. Mi, K. Urban, I. Vrejoiu, M. Alexe, and D. Hesse, Nat. Mater. **7**, 57 (2008).
[14]J. Seidel, L. W. Martin, Q. He, Q. Zhan, Y. H. Chu, A. Rother, M. E. Hawkridge, P. Maksymovych, P. Yu, M. Gajek, N. Balke, S. V. Kalinin, S. Gemming, F. Wang, G. Catalan, J. F. Scott, N. A. Spaldin, J. Orenstein, and R. Ramesh, Nat. Mater. **8**, 229 (2009).
[15]Q. H. Zhang, L. J. Wang, X. K. Wei, R. C. Yu, L. Gu, A. Hirata, M. W. Chen, C. Q. Jin, Y. Yao, Y. G. Wang, and X. F. Duan, Phys. Rev. B **85**, 020102 (2012).
[16]K. Kimoto, T. Asaka, T. Nagai, M. Saito, Y. Matsui, and K. Ishizuka, Nature **450**, 702 (2007).
[17]J. A. Mundy, J. Schaab, Y. Kumagai, A. Cano, M. Stengel, I. P. Krug, D. M. Gottlob, H. Dog Anay, M. E. Holtz, R. Held, Z. Yan, E. Bourret, C. M. Schneider, D. G. Schlom, D. A. Muller, R. Ramesh, N. A. Spaldin, and D. Meier, Nat. Mater. **16**, 622 (2017).
[18]T. Rojac, A. Bencan, G. Drazic, N. Sakamoto, H. Ursic, B. Jancar, G. Tavcar, M. Makarovic, J. Walker, B. Malic, and D. Damjanovic, Nat. Mater. **16**, 322 (2017).
[19]D. M. Evans, T. S. Holstad, A. B. Mosberg, D. R. Småbråten, P. E. Vullum, A. L. Dadlani, K. Shapovalov, Z. Yan, E. Bourret, D. Gao, J. Akola, J. Torgersen, A. T. J. van Helvoort, S. M. Selbach, and D. Meier, Nat. Mater. **19**, 1195 (2020).
[20]E. Soergel, J. Phys. D Appl. Phys. **44**, 464003 (2011).
[21]A. Gruverman, M. Alexe, and D. Meier, Nat. Commun. **10**, 1661 (2019).
[22]M. P. Murrell, M. E. Welland, S. J. O'Shea, T. M. H. Wong, J. R. Barnes, A. W. McKinnon, M. Heyns, and S. Verhaverbeke, Appl. Phys. Lett. **62**, 786 (1993).
[23]A. Avila and B. Bhushan, Crit. Rev. Solid State Mater. Sci. **35**, 38 (2010).
[24]S. Farokhipoor and B. Noheda, Phys. Rev. Lett. **107**, 127601 (2011).
[25]J. Guyonnet, I. Gaponenko, S. Gariglio, and P. Paruch, Adv. Mater. **23**, 5377 (2011).
[26]D. Meier, J. Seidel, A. Cano, K. Delaney, Y. Kumagai, M. Mostovoy, N. A. Spaldin, R. Ramesh, and M. Fiebig, Nat. Mater. **11**, 284 (2012).
[27]M. Schröder, A. Haußmann, A. Thiessen, E. Soergel, T. Woike, and L. M. Eng, Adv. Funct. Mater. **22**, 3936 (2012).
[28]W. Wu, Y. Horibe, N. Lee, S. W. Cheong, and J. R. Guest, Phys. Rev. Lett. **108**, 077203 (2012).
[29]T. Sluka, A. K. Tagantsev, P. Bednyakov, and N. Setter, Nat. Commun. **4**, 1808 (2013).
[30]Y. S. Oh, X. Luo, F.-T. Huang, Y. Wang, and S.-W. Cheong, Nat. Mater. **14**, 407 (2015).
[31]R. G. P. McQuaid, M. P. Campbell, R. W. Whatmore, A. Kumar, and J. M. Gregg, Nat. Commun. **8**, 15105 (2017).
[32]J. Schaab, I. P. Krug, F. Nickel, D. M. Gottlob, H. Doğanay, A. Cano, M. Hentschel, Z. Yan, E. Bourret, C. M. Schneider, R. Ramesh, and D. Meier, Appl. Phys. Lett. **104**, 232904 (2014).
[33]J. Schaab, M. Trassin, A. Scholl, A. Doran, Z. Yan, E. Bourret, R. Ramesh, and D. Meier, J. Phys. Conf. Ser. **592**, 012120 (2015).
[34]A. S. Pawlik, T. Kämpfe, A. Haußmann, T. Woike, U. Treske, M. Knupfer, B. Büchner, E. Soergel, R. Streubel, A. Koitzsch, and L. M. Eng, Nanoscale **9**, 10933 (2017).
[35]J. Schaab, K. Shapovalov, P. Schoenherr, J. Hackl, M. I. Khan, M. Hentschel, Z. Yan, E. Bourret, C. M. Schneider, S. Nemsák, M. Stengel, A. Cano, and D. Meier, Appl. Phys. Lett. **115**, 122903 (2019).
[36]C. Becher, L. Maurel, U. Aschauer, M. Lilienblum, C. Magén, D. Meier, E. Langenberg, M. Trassin, J. Blasco, I. P. Krug, P. A. Algarabel, N. A. Spaldin, J. A. Pardo, and M. Fiebig, Nat. Nanotechnol. **10**, 661 (2015).

© Author(s) 2020

[37]G. F. Nataf, P. Grysan, M. Guennou, J. Kreisel, D. Martinotti, C. L. Rountree, C. Mathieu, and N. Barrett, Sci. Rep. **6**, 33098 (2016).
[38]J. Schaab, I. P. Krug, H. Doğanay, J. Hackl, D. M. Gottlob, M. I. Khan, S. Nemšák, L. Maurel, E. Langenberg, P. A. Algarabel, J. A. Pardo, C. M. Schneider, and D. Meier, Phys. Rev. Appl. **5**, 054009 (2016).
[39]G. F. Nataf, M. Guennou, J. Kreisel, P. Hicher, R. Haumont, O. Aktas, E. K. H. Salje, L. Tortech, C. Mathieu, D. Martinotti, and N. Barrett, Phys. Rev. Mater. **1**, 074410 (2017).
[40]E. Bauer, Rep. Prog. Phys. **57**, 895 (1994).
[41]G. Y. Robinson and R. M. White, Appl. Phys. Lett. **10**, 320 (1967).
[42]K. P. Meyer, H. Blumtritt, and L. Szcześniak, Ultramicroscopy **6**, 67 (1981).
[43]V. V. Aristov, L. S. Kokhanchik, and Y. I. Voronovskii, Phys. Status Solidi A **86**, 133 (1984).
[44]A. K. Tagantsev, L. E. Cross, and J. Fousek, *Domains in Ferroic Crystals and Thin Films* (Springer, New York, 2010).
[45]A. Lubk, S. Gemming, and N. A. Spaldin, Phys. Rev. B **80**, 104110 (2009).
[46]D. Lee, R. K. Behera, P. Wu, H. Xu, Y. L. Li, S. B. Sinnott, S. R. Phillpot, L. Q. Chen, and V. Gopalan, Phys. Rev. B **80**, 060102 (2009).
[47]P. Mokrý, A. K. Tagantsev, and J. Fousek, Phys. Rev. B **75**, 094110 (2007).
[48]E. A. Eliseev, A. N. Morozovska, G. S. Svechnikov, V. Gopalan, and V. Y. Shur, Phys. Rev. B **83**, 235313 (2011).
[49]M. Y. Gureev, A. K. Tagantsev, and N. Setter, Phys. Rev. B **83**, 184104 (2011).
[50]P. S. Bednyakov, B. I. Sturman, T. Sluka, A. K. Tagantsev, and P. V. Yudin, npj Comput. Mater. **4**, 65 (2018).
[51]G. F. Nataf, N. Guennou, J. M. Gregg, D. Meier, J. Hlinka, E. K. H. Salje, and J. Kreisel, Nat. Rev. Phys. **2**, 634 (2020).
[52]A. Q. Jiang and Y. Zhang, NPG Asia Mater. **11**, 2 (2019).
[53]E. Soergel, Appl. Phys. B **81**, 729 (2005).
[54]G. F. Nataf and M. Guennou, J. Phys. Condens. Matter **32**, 183001 (2020).
[55]J. P. Doughert, E. Sawaguch, and L. E. Cross, Appl. Phys. Lett. **20**, 364 (1972).
[56]M. šafránková, J. Fousek, and S. A. KiŽaev, Czech. J. Phys. B **17**, 559 (1967).
[57]S. M. Griffin, M. Lilienblum, K. T. Delaney, Y. Kumagai, M. Fiebig, and N. A. Spaldin, Phys. Rev. X **2**, 041022 (2012).
[58]Q. N. Meier, M. Lilienblum, S. M. Griffin, K. Conder, E. Pomjakushina, Z. Yan, E. Bourret, D. Meier, F. Lichtenberg, E. K. H. Salje, N. A. Spaldin, M. Fiebig, and A. Cano, Phys. Rev. X **7**, 041014 (2017).
[59]T. Choi, Y. Horibe, H. T. Yi, Y. J. Choi, W. Wu, and S. W. Cheong, Nat. Mater. **9**, 253 (2010).
[60]Y. Geng, N. Lee, Y. J. Choi, S. W. Cheong, and W. Wu, Nano Lett. **12**, 6055 (2012).
[61]J. Schaab, S. H. Skjærvø, S. Krohns, X. Dai, M. E. Holtz, A. Cano, M. Lilienblum, Z. Yan, E. Bourret, D. A. Muller, M. Fiebig, S. M. Selbach, and D. Meier, Nat. Nanotechnol. **13**, 1028 (2018).
[62]K. W. Urban, Science **321**, 506 (2008).
[63]Y. Yu, X. Zhang, Y. G. Zhao, N. Jiang, R. Yu, J. W. Wang, C. Fan, X. F. Sun, and J. Zhu, Appl. Phys. Lett. **103**, 032901 (2013).
[64]M. E. Holtz, K. Shapovalov, J. A. Mundy, C. S. Chang, Z. Yan, E. Bourret, D. A. Muller, D. Meier, and A. Cano, Nano Lett. **17**, 5883 (2017).
[65]J. Nordlander, M. Campanini, M. D. Rossell, R. Erni, Q. N. Meier, A. Cano, N. A. Spaldin, M. Fiebig, and M. Trassin, Nat. Commun. **10**, 5591 (2019).
[66]V. K. Zworykin, J. Hillier, and R. L. Snyder, ASTM Bull. **117**, 15 (1942).
[67]*Electron Microscopy of Polymers*, edited by G. H. Michler (Springer, Berlin, 2008), pp. 87–120.
[68]L. Reimer, *Scanning Electron Microscopy*, 2nd ed. (Springer-Verlag, Berlin, 1998).
[69]R. Le Bihan, Ferroelectrics **97**, 19 (1989).
[70]N. Nakatani, Jpn. J. Appl. Phys. **12**, 1723 (1973).
[71]M. Maussion, M. Polomska, and R. L. Bihan, Ferroelectr. Lett. Sect. **6**, 41 (1986).
[72]R. F. Egerton, *Physical Principles of Electron Microscopy* (Springer, 2005).
[73]H. Seiler, J. Appl. Phys. **54**, R1 (1983).
[74]B. J. Griffin, Scanning **33**, 162 (2011).
[75]J. Cazaux, J. Appl. Phys. **59**, 1418 (1986).
[76]P. Hirsch, M. Kässens, M. Püttmann, and L. Reimer, Scanning **16**, 101 (1994).
[77]A. Sogr, A. Maslovskaya, and I. Kopylova, Ferroelectrics **341**, 29 (2006).
[78]N. Alyabyeva, A. Ouvrard, I. Lindfors-Vrejoiu, O. Ageev, and D. McGrouther, Appl. Phys. Lett. **111**, 222901 (2017).
[79]J. F. Ihlefeld, J. R. Michael, B. B. McKenzie, D. A. Scrymgeour, J.-P. Maria, E. A. Paisley, and A. R. Kitahara, J. Mater. Sci. **52**, 1071 (2017).
[80]X. Li, K. Terabe, H. Hatano, and K. Kitamura, Jpn. J. Appl. Phys. **45**, L399 (2006).
[81]O. Bak, T. S. Holstad, Y. Tan, H. Lu, D. M. Evans, K. A. Hunnestad, B. Wang, J. P. V. McConville, P. Becker, L. Bohatý, I. Lukyanchuk, V. M. Vinokur, A. T. J. van Helvoort, J. M. Gregg, L.-Q. Chen, D. Meier, and A. Gruverman, Adv. Funct. Mater. **30**, 2000284 (2020).
[82]E. Vlasov, D. Chezganov, M. Chuvakova, and V. Y. Shur, Scanning **2018**, 1.
[83]L. S. Kokhanchik, Phys. Solid State **60**, 1778 (2018).
[84]J. A. Hooton and W. J. Merz, Phys. Rev. **98**, 409 (1955).
[85]R. Le Bihan and M. Maussion, J. Physique **33**, C2-C215 (1972).
[86]A. A. Sogr, Ferroelectrics **97**, 47 (1989).
[87]G. Rosenman, A. Skliar, I. Lareah, N. Angert, M. Tseitlin, and M. Roth, Phys. Rev. B **54**, 6222 (1996).
[88]N. Domingo, E. Pach, K. Cordero-Edwards, V. Pérez-Dieste, C. Escudero, and A. Verdaguer, Phys. Chem. Chem. Phys. **21**, 4920 (2019).
[89]I. Krug, N. Barrett, A. Petraru, A. Locatelli, T. O. Mentes, M. A. Niño, K. Rahmanizadeh, G. Bihlmayer, and C. M. Schneider, Appl. Phys. Lett. **97**, 222903 (2010).
[90]A. B. Mosberg, E. D. Roede, D. M. Evans, T. S. Holstad, E. Bourret, Z. Yan, A. T. J. van Helvoort, and D. Meier, Appl. Phys. Lett. **115**, 122901 (2019).
[91]L. Kokhanchik and D. Irzhak, Ferroelectrics **352**, 134 (2007).
[92]L. S. Kokhanchik, Micron **40**, 41 (2009).
[93]L. A. Giannuzzi and F. A. Stevie, Micron **30**, 197 (1999).
[94]S. Reyntjens and R. Puers, J. Micromech. Microeng. **11**, 287 (2001).
[95]N. Yao, *Focused Ion Beam Systems: Basics and Applications* (Cambridge University Press, 2007).
[96]L. J. McGilly, P. Yudin, L. Feigl, A. K. Tagantsev, and N. Setter, Nat. Nanotechnol. **10**, 145 (2015).
[97]S. R. Burns, J. M. Gregg, and V. Nagarajan, Adv. Funct. Mater. **26**, 8367 (2016).
[98]I. Utke, P. Hoffmann, and J. Melngailis, J. Vac. Sci. Technol. B **26**, 1197 (2008).
[99]A. Botman, J. J. Mulders, and C. W. Hagen, Nanotechnology **20**, 372001 (2009).
[100]M. Schaffer, B. Schaffer, and Q. Ramasse, Ultramicroscopy **114**, 62 (2012).
[101]R. G. P. McQuaid, L. J. McGilly, P. Sharma, A. Gruverman, and J. M. Gregg, Nat. Commun. **2**, 404 (2011).
[102]J. R. Whyte and J. M. Gregg, Nat. Commun. **6**, 7361 (2015).
[103]T. Nagata, Y. Sakuma, M. Haemori, K. Nakajima, R. Kometani, K. Kanda, S. Matsui, and T. Chikyow, Jpn. J. Appl. Phys. **47**, 9010 (2008).
[104]T. F. Kelly and M. K. Miller, Rev. Sci. Instrum. **78**, 031101 (2007).
[105]I. M. Robertson, C. A. Schuh, J. S. Vetrano, N. D. Browning, D. P. Field, D. J. Jensen, M. K. Miller, I. Baker, D. C. Dunand, R. Dunin-Borkowski, B. Kabius, T. Kelly, S. Lozano-Perez, A. Misra, G. S. Rohrer, A. D. Rollett, M. L. Taheri, G. B. Thompson, M. Uchic, X. L. Wang, and G. Was, J. Mater. Res. **26**, 1341 (2011).
[106]B. Gault, M. P. Moody, J. M. Cairney, and S. P. Ringer, *Atom Probe Microscopy* (Springer-Verlag, New York, 2012).
[107]M. K. Miller and R. G. Forbes, *Atom-Probe Tomography* (Springer, Boston, MA, 2014).
[108]A. Devaraj, D. E. Perea, J. Liu, L. M. Gordon, T. J. Prosa, P. Parikh, D. R. Diercks, S. Meher, R. P. Kolli, Y. S. Meng, and S. Thevuthasan, Int. Mater. Rev. **63**, 68 (2018).
[109]E. Talbot, R. Lardé, P. Pareige, L. Khomenkova, K. Hijazi, and F. Gourbilleau, Nanoscale Res. Lett. **8**, 39 (2013).
[110]R. Kirchhofer, D. R. Diercks, B. P. Gorman, J. F. Ihlefeld, P. G. Kotula, C. T. Shelton, and G. L. Brennecka, J. Am. Ceram. Soc. **97**, 2677 (2014).

© Author(s) 2020

[111]S. Jiang, H. Wang, Y. Wu, X. Liu, H. Chen, M. Yao, B. Gault, D. Ponge, D. Raabe, A. Hirata, M. Chen, Y. Wang, and Z. Lu, Nature **544**, 460 (2017).
[112]K. Thompson, D. Lawrence, D. J. Larson, J. D. Olson, T. F. Kelly, and B. Gorman, Ultramicroscopy **107**, 131 (2007).
[113]A. K. Kambham, A. Kumar, M. Gilbert, and W. Vandervorst, Ultramicroscopy **132**, 65 (2013).
[114]J. Lee and J.-P. Ahn, Appl. Microsc. **46**, 14 (2016).
[115]M. K. Miller and R. G. Forbes, *Atom-probe Tomography* (Springer US, 2014).
[116]J. Luo, J. Materiomics **1**, 22 (2015).
[117]V. Ravikumar, R. P. Rodrigues, and V. P. Dravid, Phys. Rev. Lett. **75**, 4063 (1995).
[118]X. Xu, Y. Liu, J. Wang, D. Isheim, V. P. Dravid, C. Phatak, and S. M. Haile, Nat. Mater. **19**, 887 (2020).
[119]V. Ravikumar, R. P. Rodrigues, and V. P. Dravid, J. Am. Ceram. Soc. **80**, 1131 (1997).

© Author(s) 2020